small
NANO MICRO
www.small-journal.com

Design of 3D Graphene-Oxide Spheres and Their Derived Hierarchical Porous Structures for High Performance Supercapacitors

Zhuangnan Li, Srinivas Gadipelli, Yuchen Yang, and Zhengxiao Guo**

Graphene-oxide (GO) based porous structures are highly desirable for supercapacitors, as the charge storage and transfer can be enhanced by advancement in the synthesis. An effective route is presented of, first, synthesis of three-dimensional (3D) assembly of GO sheets in a spherical architecture (GOS) by flash-freezing of GO dispersion, and then development of hierarchical porous graphene (HPG) networks by facile thermal-shock reduction of GOS. This leads to a superior gravimetric specific capacitance of ≈306 F g^{-1} at 1.0 A g^{-1}, with a capacitance retention of 93% after 10 000 cycles. The values represent a significant capacitance enhancement by 30–50% compared with the GO powder equivalent, and are among the highest reported for GO-based structures from different chemical reduction routes. Furthermore, a solid-state flexible supercapacitor is fabricated by constructing the HPG with polymer gel electrolyte, exhibiting an excellent areal specific capacitance of ≈220 mF cm^{-2} at 1.0 mA cm^{-2} with exceptional cyclic stability. The work reveals a facile but efficient synthesis approach of GO-based materials to enhance the capacitive energy storage.

1. Introduction

Supercapacitors, or electrochemical capacitors, offer great potential for large-scale energy storage due to their unique advantages of rapid charge–discharge rate, long cycle life, and ultrahigh power density (10 kW kg^{-1}).[1] Those are ideal for fast energy storage and delivery, e.g., for smart power grids and hybrid electric vehicles.[2] However, their energy density (3–5 Wh kg^{-1}) is relatively low, compared with the traditional batteries (25–35 Wh kg^{-1}). In order to boost their performance, efforts have been devoted to increase the specific capacitance of the electrode material, both in terms of the power and the energy densities. In general, the specific capacitance (gravimetric and volumetric) of an electrode material is influenced directly by its surface functionality, specific surface area, pore volume, and pore size distribution, which allows efficient charge transport and storage.[3] In addition, the intrinsic density of the electrode and the electrical conductivity play a critical role in achieving a high volumetric capacitance and rate capability.[4] Therefore, significant research has been focused on materials design via synthesis techniques of top-down and bottom-up approaches.[5,6] A wide spectrum of solids have been investigated including metal-oxide/hydroxide complexes, supported metallic adducts of oxides, nitrides, phosphides, and sulphides, and inorganic porous structures of polymers, metal–organic frameworks (MOFs), biomass, and the family of carbon nanostructures.[7–13]

Porous structures with heteroatom dopants and implanted metal-complexes are highly desirable, due to their superior capability for tuning ion accessible porosity, surface chemistry, and chemical stability.[14] The best examples are carbon based-nanostructures, which are also highly abundant and can be readily synthesized and scaled up.[15] Specifically, the desirable porosity, density, and surface functionality can be tailored by the selection of appropriate carbon precursors and synthesis techniques. For instance, porous carbons with ultrahigh specific surface area, generated by chemical activation of biomass or petroleum pitch, show largely enhanced energy storage.[8,16] Similarly, the bottom-up design of porous frameworks (coordinated polymers, MOFs, biomass, etc.) derived carbons yields multifunctional features, leading to ultrahigh specific capacitance, where a major contributing factor is the pseudocapacitance of the surface functional groups.[17]

In recent years, graphene-oxide (GO) based carbons have emerged as promising electrode materials for electrochemical energy storage and conversion devices owing to their highly tunable surface chemistry.[18–20] The top-down synthesis of GO precursor from graphite is a viable method for further development of functional porous structures.[21] In this context, processing of GO is the key factor and can yield outstanding multifunctional structural features.[20] For example, layered materials with tunable interlayer spacing can be designed by the introduction of pillaring moieties and/or the reduction of surface lamellar oxygen groups under controlled chemical or thermal treatment.[22–26] Such techniques yield a densely packed structure with relatively low porosity. Further advancement in their structural characteristics has been achieved by solution-processing of GO, including hydrothermal/solvothermal curing, filtration, chemical reduction, and activation.[27–30]

Z. Li, Dr. S. Gadipelli, Y. Yang, Prof. Z. X. Guo
Department of Chemistry
University College London
20 Gordon Street, London WC1H 0AJ, UK
E-mail: gsrinivasphys@gmail.com; z.x.guo@ucl.ac.uk

DOI: 10.1002/smll.201702474

Direct solid-state exfoliation by microwave and thermal shock has also been applied.[31–35] Typical gravimetric capacitance (≈250 F g^{-1}) of such structures is still less than the theoretical value of 550 F g^{-1} due to the strong overlapping/aggregation of graphene layers via π–π aromatic interactions, thus leading to reduced accessibility of the interlayer spacing.[36–39] Considerable efforts have been devoted to minimize the aggregation. For instance, sacrificial templates were utilized as a backbone to prepare hierarchical structures.[40,41] In addition, different types of molecular nanostructures were inserted between graphene sheets as spacers to facilitate charge transport and storage.[42–44]

Apart from surface area, pore volume and pore-size distribution across micropore (<2 nm), mesopore (2–50 nm), and macropore (>50 nm) regimes (a hierarchical pore structure) play a crucial role in facilitating ion storage, transport, and distribution.[45] A highly porous structure can provide sufficient pore volume with micropores and mesopores for charge adsorption and ion transport.[46] Evidently, aggregation of layers limits the true charge capacity.[47,48] Here, we report a method of producing three-dimensional (3D) assembly of GO sheets by flash-freezing the droplets of GO dispersion directly in liquid nitrogen (at 77 K). The idea is to retain the separation and random orientations of the GO sheets in a diluted liquid phase. Thus, the subsequent freeze-drying leads to GO spheres (GOS) of 2–3 mm diameter. Such GOS samples synthesized at various concentrations of GO in the solution show distinctly different structural characteristics to that of precursor, GO. Therefore, the supercapacitors designed from the GOS sample exhibit a highly enhanced charge storage capacity of 30–50% compared to the GO powder sample, when processed under similar thermal reduction conditions. Specifically, the thermal-shock of GOS (at ≈400 °C in less than 5 min) derived hierarchical porous graphene (HPG) networks shows an excellent specific capacitance of ≈306 F g^{-1} (at 1.0 A g^{-1} in 1.0 M KOH electrolyte) and a long-term cyclic stability with a capacitance retention of >93% after 10 000 cycles. The reported gravimetric specific capacitance of over 300 F g^{-1} at 1.0 A g^{-1} in our HPG is clearly higher to many other GO-based structures in the literature. Moreover, the HPG-based solid-state flexible supercapacitor exhibits an impressive areal specific capacitance of 220 mF cm^{-2} at 1 mA cm^{-2} and cyclic capacity retention of ≈90% after 5000 cycles.

2. Results and Discussion

Figure 1a shows schematically the typical synthesis procedures for 3D assembled GO sheets via flash-freezing. First, precursor GO was synthesized from a synthetic graphite powder (<20 µm) by an improved Hummers' method (see the Experimental Section). Then, the GO sheets were fully dispersed in water at different concentrations (2, 4, and 10 mg mL^{-1}) by ultrasonication. Naturally, these delaminated GO sheets distribute very differently in the solution compared to their 2D packed form in

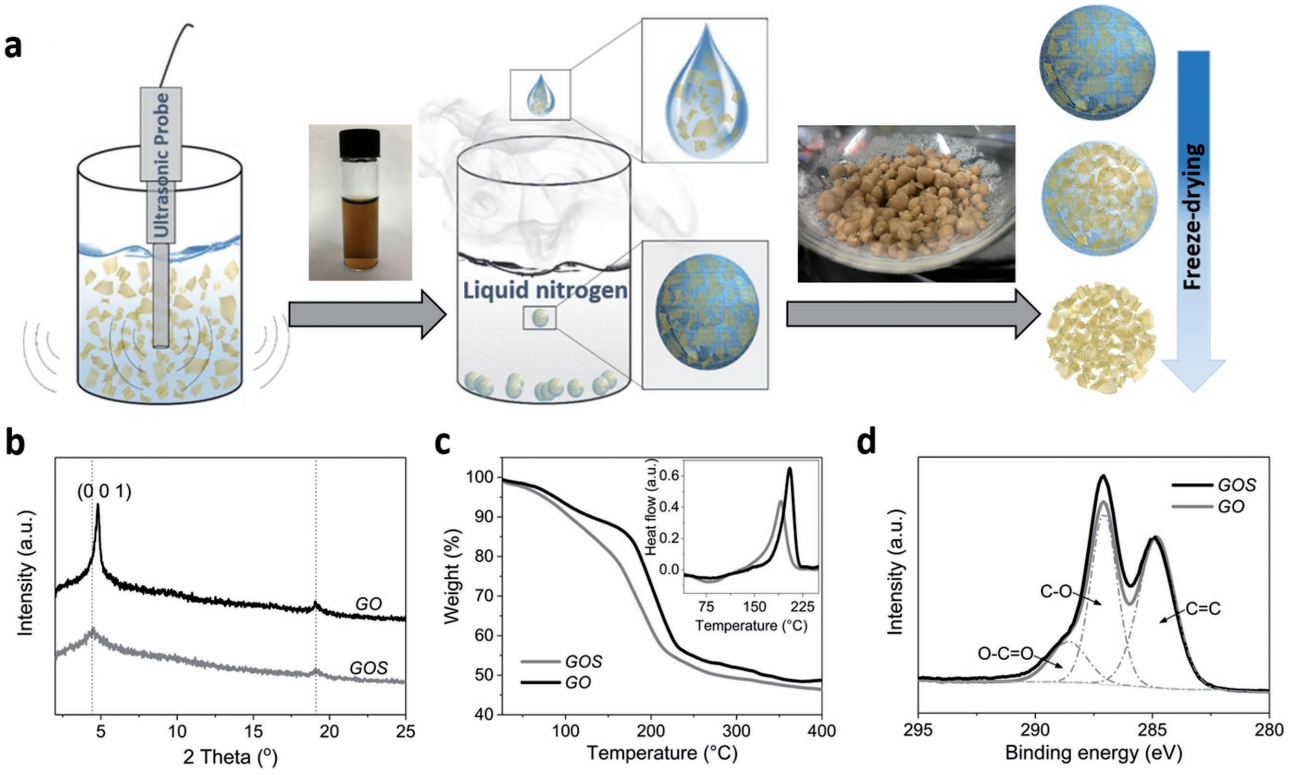

Figure 1. Preparation and structural characteristics of graphene-oxide spheres (GOS). a) Schematic illustration of the preparation procedure for GOS. From left to right: Obtaining GO solution under ultrasonication; Photograph: formed 2 mg mL^{-1} GO aqueous solution; Droplet of GO solution into liquid nitrogen (77 K) by pipette; Photograph: formed GOS after dropped into liquid nitrogen; Freeze-drying of GOS. b) PXRD (Mo-Kα radiation) patterns of GO and GOS. c) TGA and DSC (inset) curves of GO and GOS. d) XPS C 1s spectra of GO and GOS.

bulk solid-state.[49,50] The abundant oxygen-containing surface functional groups, such as epoxides, hydroxyls, and carboxyls (Figure S1, Supporting Information), make the GO highly hydrophilic, thus easily producing a homogeneous GO dispersion. Subsequently, the GO solution was dropped into liquid nitrogen (77 K) with a 2 mm diameter pipette. The randomly oriented GO sheets were rapidly entrapped in the ice skeleton of the frozen droplets. The ice crystals formed during the freezing process act as spacers among GO sheets, thus preventing them from aggregation. The size of the sphere and the free-volume among the GO sheets can be tuned by the size of droplets and the concentration of GO in the solution, respectively. Spheres obtained at a suitable concentration can yield fully isolated GO sheets, assembled in highly random orientations. In order to obtain a homogeneous 3D assembly, one needs to control the volume of liquid or droplet-size and the speed of dropping, this is to compromise with the high specific heat capacity of water (see the Experimental section). Finally, the GOS were obtained after careful freeze-drying to remove ice crystals via sublimation without disturbing the formed 3D assembly of GO.

Powder X-ray diffraction (PXRD) patterns (Figure 1b) of samples show the (0 0 1) characteristic peak at $2\theta = \approx 4.8°$, with a corresponding *c*-axis d-spacing of ≈0.85 nm (derived by Bragg's equation for the Mo Kα radiation), which is more than double to the interlayer spacing of 0.344 nm in graphite (Figure S2, Supporting Information). The obviously weaker and broader nature of such characteristic (0 0 1) peak in GOS suggests a 3D assembly of GO sheets in a turbostratic orientation.[51] Thermogravimetric analysis (TGA) (Figure 1c) exhibits severe mass loss at around 200 °C due to the decomposition of the actual structure, containing different oxygen functional groups (—C—O—C, —C—OH, and —COOH) in the form of CO/CO_2. Here, it is worth noting that the decomposition of the structures is associated with exothermic reaction (see the inset differential scanning calorimetry, DSC curves), due to the disproportionation reactions of carbon atoms.[52] Comparatively, more mass loss (between 100 and 150 °C) and less thermal stability (≈25 °C) in the GOS further indicates the more structure bound water molecules in their 3D layers and a reduced degree of stacking, which is indicated by a more pronounced endothermic peak of GOS at ≈90 °C in DSC curves. This can be also evidenced by the comparatively increased oxygen content in X-ray photoemission spectroscopy (XPS) spectra (Figure 1d; Table S1, Supporting Information). TGA curves also show the explosive decomposition of GO sample compared with GOS, when performed the tests under similar conditions and for the same given amount (10 mg) of sample packed in 70 µL volume of alumina sample crucible (Figure S3, Supporting Information). The void spaces in the 3D graphene layers of GOS can work as channels to readily escape decomposed volatile surface functional groups. On the contrary, due to the diffusion/kinetics limitation pertaining to the 2D stacked layers in the GO sample, the structure has to undergo huge pressure and thus exfoliation occurs. These structural characteristics are also well supported by morphology and gas uptake measurement (Figures S4 and S5, Supporting Information), in which GOS sample shows an enhanced specific surface area compared with stacked layers in GO.

Next, these GO and GOS samples were reduced by simple thermal treatment (with a slow heating rate of 2 °C min^{-1}, to prevent the exfoliation, and are respectively named as *sr*GO and *sr*GOS) and examined the supercapacitor properties (Experimental Section). Details of XPS results for various *sr*GOS samples are provided in Figure S6 and Table S1 (Supporting Information). Cyclic voltammetry (CV) curves at a scan rate of 10 mV s^{-1} display a combined electrochemical double layer capacitor and pseudocapacitor behavior (**Figure 2**a; Figure S7, Supporting Information). This is also evidenced by the quasi-triangular shape of the galvanostatic charge/discharge

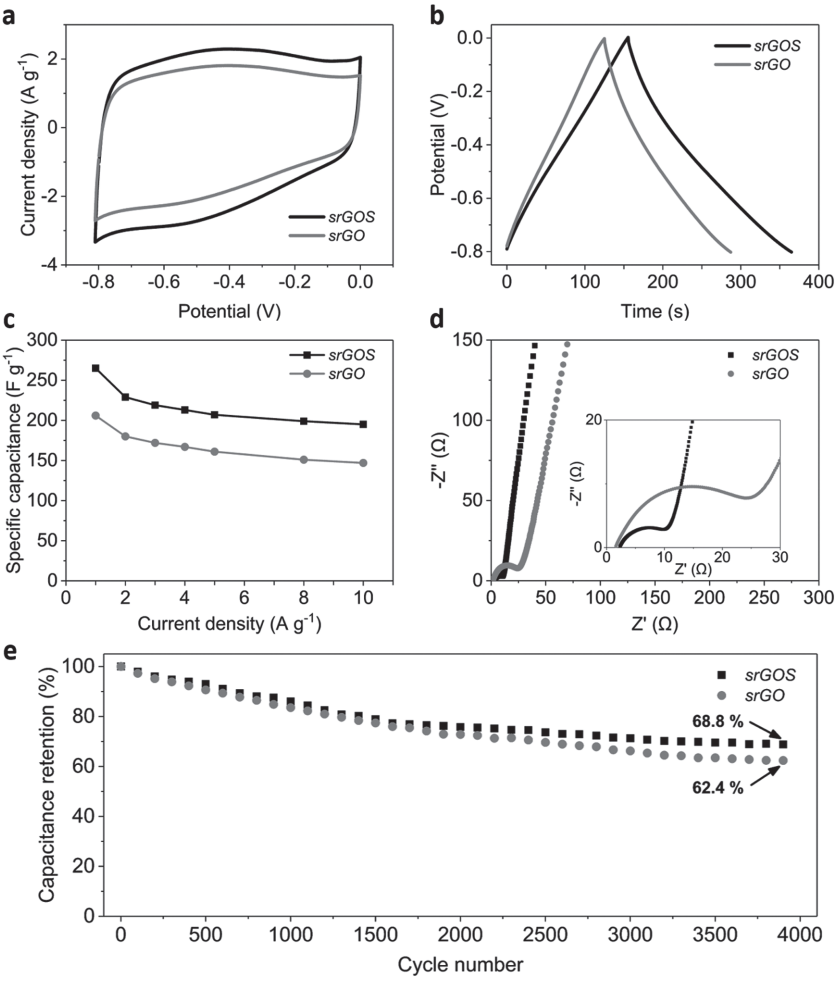

Figure 2. Supercapacitor performance of *sr*GO and *sr*GOS in 1.0 M KOH aqueous electrolyte. a) CV curves at the scan rate of 10 mV s^{-1}. b) Galvanostatic charge/discharge curves at 1.0 A g^{-1}. c) Comparison of specific capacitance at different current densities derived from the discharge curves. d) Nyquist plot. Inset: magnified view of the high-frequency region. e) Cyclic stability for 4000 cycles at the current density of 5.0 A g^{-1}.

curves (Figure 2b). In a constant potential window (ΔV), a longer time of discharge (Δt) at constant applied current (I) yields a higher charge storage capacity in the sample (according to $C = I \times \Delta t/\Delta V$). Accordingly, *sr*GOS electrode exhibits a superior specific capacitance of 265 F g^{-1} at 1.0 A g^{-1}, compared with 206 F g^{-1} in the *sr*GO electrode, under identical current density. The specific capacitance of each sample at different current densities is shown in Figure 2c (and Table S2, Supporting Information). As can be seen, *sr*GOS electrode exhibits about 30% higher capacitance compared to *sr*GO electrode and also shows a good rate capability of 195 F g^{-1} at 10.0 A g^{-1}. Such enhancement in the capacitance can be directly attributed to the efficient ion transport in the sample. This behavior is further demonstrated in detail by electrochemical impedance spectroscopy (EIS) (Figure 2d). Nyquist plot with a more vertical slope at the low frequency region suggests further ideal capacitive behavior for *sr*GOS. At the high frequency region (inset of Figure 2d), comparatively smaller diameter of semicircle and shorter 45° Warburg region indicates a better diffusion of electrolyte and lower resistance of charge transport in the *sr*GOS sample.

The other important characteristic of supercapacitors is a long-term cyclic stability, i.e., the ability to retain the capacitance for the thousands of charge–discharge cycles. As shown in Figure 2e, the *sr*GOS exhibits a large drop in capacitance to 31% within the first 4000 cycles, which is slightly better than the 38% drop in *sr*GO, but is relatively poor compared with other carbon-based structures.[4,30,46] Such capacitance stability degradation can be directly ascribed to pseudocapacitance introduced by excess surface oxygen-containing functional groups, and charge losses caused by internal and charge transport resistances.[49] Unlike double-layer capacitance which only involves the charge rearrangement, the pseudocapacitance is related to redox reactions, such as: >C−OH ↔ C−O + H^+ + e^-, −COOH ↔ −COO + H^+ + e^-, and >C−O + e^- ↔ >C−O^-.[10,46] However, some of those chemical reactions are irreversible and thermodynamically unstable during the long-term cycling and hence diminish the performance.[53] To further confirm this, the partly reduced *sr*GOS sample (*sr*GOS@200) with more oxygen content (>19 at%) at lower reduction temperature of 200 °C was synthesized and measured (Figure S8, Supporting Information). Clearly, the enhanced surface oxygen group contribution can be seen with appearance of prominent redox peaks in CV thus leading to additional capacitance, reaching 290 F g^{-1} at 1.0 A g^{-1}. Note that this value is about 25 F g^{-1} higher to the *sr*GOS (with an oxygen content of ≈15.8 at%). However, as attributed, the specific capacitance of *sr*GOS@200 sample shows a rapid deterioration in cyclic test, reduced by 45.0% within 4000 cycles. Moreover, the Nyquist plot also indicates a poor ion transport capability in the *sr*GOS@200 sample with a higher oxygen content. Note that the higher reduction leads to more stable cyclic performance, but it comes at the expense of the capacitance (Figure S8, Supporting Information).

Therefore, a further efficient reduction route is needed for simultaneously enhancing the overall energy storage capability: specific capacitance, cyclic stability, and charge transport/distribution. Thermal-shock is an ideal reduction strategy as GO decomposition is associated with large exothermic heat release, which in combination largely enhances the sudden volatility of the surface oxygen groups to create a substantial level of internal pressure, further props-up the GO sheets.[34] Therefore, the thermal-shock of GOS, conducted at 400 °C (in a preheated furnace) for less than 5 min, eventually produced a highly hierarchical porous graphene networks with a further enhanced degree of reduction (**Figure 3**; Figures S2 and S9,

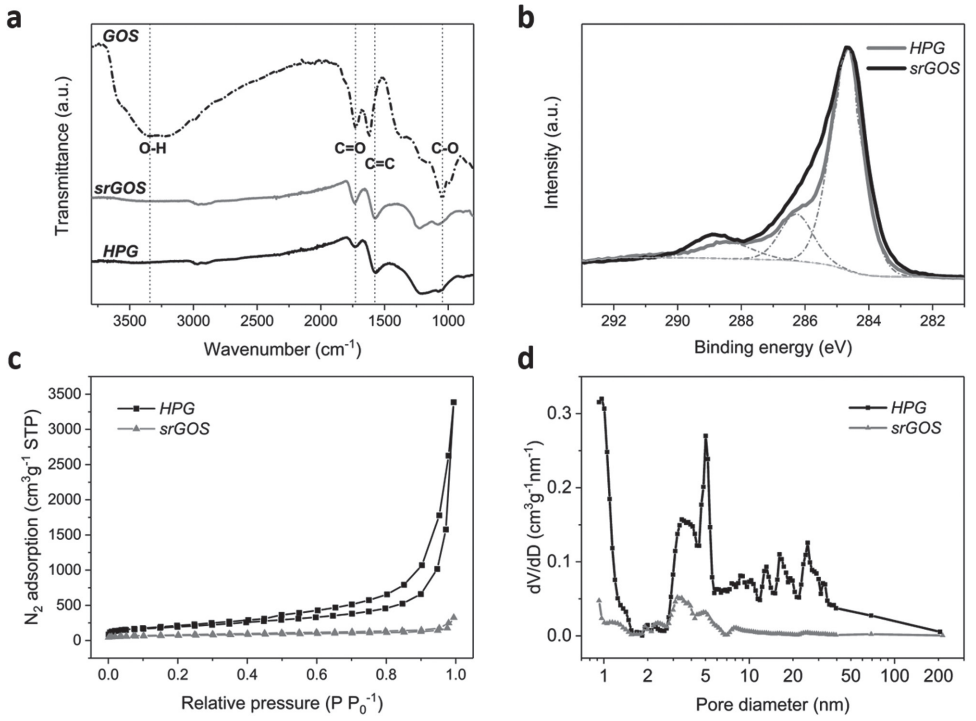

Figure 3. Structural characteristics of thermally reduced GOS samples. a) FTIR spectra with respect to the precursor, GOS. b) XPS C 1s spectra. c) N_2 adsorption–desorption isotherm at 77 K. d) Pore size distribution curves.

Supporting Information). For instance, Fourier transform infrared (FTIR) and XPS spectra show comparatively more reduction in HPG over *sr*GOS (Figure 3a,b). The C/O ratio is increased to ≈6.5 in HPG compared to ≈5.2 in *sr*GOS, with respective oxygen content of ≈13.0 and ≈16.0 at%. Specifically, the porosity characteristics (specific surface area, pore volume, and pore size distribution[54]) reveal a highly hierarchical porous nature in HPG (Figure 3 c,d), yielding a specific surface area and a total pore volume of 695 $m^2\ g^{-1}$ and 5.2 $cm^3\ g^{-1}$, respectively, compared to 278 $m^2\ g^{-1}$ and 0.5 $cm^3\ g^{-1}$ in the *sr*GOS. Moreover, the HPG sample also exhibits a wide pore-size distribution and pore development at both the micropore and narrow mesopore regions with corresponding pore volumes of 0.11 and 3.44 $cm^3\ g^{-1}$ respectively, comparatively higher than the *sr*GOS (0.07 and 0.23 $cm^3\ g^{-1}$). A considerable macropore volume of ≈2.0 $cm^3\ g^{-1}$ is also seen in HPG sample. Worth noting that the porosity in our HPG derived from GOS is higher than those previously reported thermal-shock reduced GO structures.[48]

Surface morphology by scanning electron microscopy and transmission electron microscopy (SEM and TEM) further illustrates the differences between *sr*GOS and HPG samples (**Figure 4**; Figure S10, Supporting Information). A clear change in layered morphologies can be seen from precursor *sr*GO to *sr*GOS and HPG samples. The heavily stacked GO platelets are delaminated into single/few layers in *sr*GOS (Figure 4a,b). Moreover, the *sr*GOS shows folded layers with extensive wrinkles, maybe which can prevent them from forming strong aggregation.[50] A further exfoliation induced graphenic networks can be seen in the HPG. TEM images of HPG also reveal a highly interconnected structure, which is in good agreement with SEM results (Figure 4c–f).

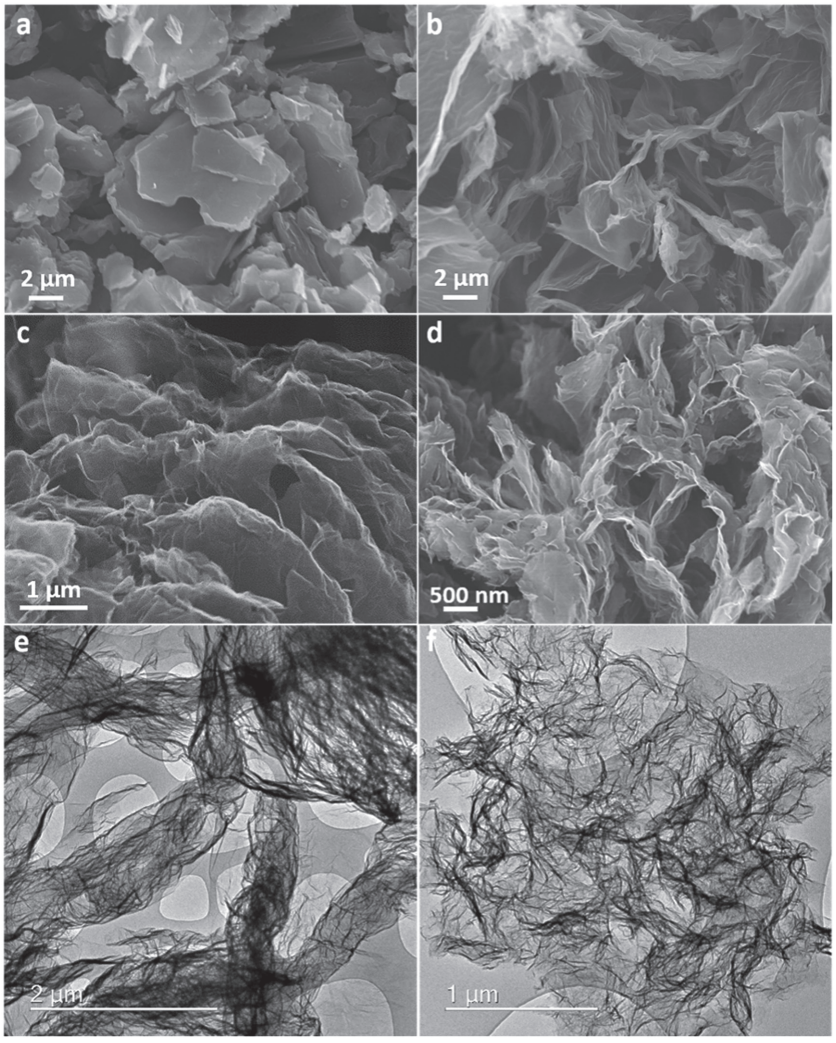

Figure 4. Morphology of thermally reduced GOS samples. a–d) SEM and e,f) TEM images of *sr*GO (a), *sr*GOS (b), and HPG (c–f) at different magnifications.

Such combination of unique structural characteristics of HPG with highly exposed surface area and pore accessibility can synergistically yield enhanced double-layer supercapacitor performance (**Figure 5**; Figures S11 and S12, Supporting Information). Thus, the HPG electrode exhibits a superior specific capacitance of 306 $F\ g^{-1}$ at 1.0 $A\ g^{-1}$ (Figure 5a,b). To the best of our knowledge, the gravimetric specific capacitance of over 300 $F\ g^{-1}$ at 1.0 $A\ g^{-1}$ is one of the best values among many GO-based structures, reported so far (Table S3, Supporting Information). Most of the literature shows capacitance of around 150–250 $F\ g^{-1}$ at equivalent or even lower current densities. Here, it is worth noting that *sr*GO powder or *sr*GOS shows a maximum capacitance of about 200 or 260 $F\ g^{-1}$. Furthermore, the HPG sample exhibits a significantly improved cyclic stability, which retains 93% of its initial value after 10 000 cycles (Figure 5c). The better charge transport properties in HPG sample are clearly evidenced in EIS (Figure 5d). Briefly, in addition to the higher slope in the low-frequency region, the ultrasmall semicircle in high-frequency region suggesting a greatly enhanced ionic and charge transport behavior. The increased ion migration is also evidenced by Bode plot (Figure S11, Supporting Information). At the phase angle of −45°, where the capacitive and resistive impedances are equal, HPG yields a characteristic frequency (f_0) of 0.37 Hz, which corresponds to a relaxation time constant ($\tau_0 = 1/f_0$) of 2.7 s. Note that this value is comparatively lower to 8.3 s in *sr*GOS and the traditional activated carbons (≈10 s).[55] All these characteristics indicate a faster frequency response and enhanced ion transport in the HPG sample.

We also note that the concentration of GO in the dispersion to obtain GOS samples, 2 $mg\ mL^{-1}$ (GOS) to 10 $mg\ mL^{-1}$ (GOS-10), leads to interesting structure–performance relationship (Figure 5d,e). From the PXRD patterns and SEM micrographs it is understood that layers become denser and tend to stack together with increasing concentration of GO, i.e., when going from sample GOS to GOS-10 (Figure 5f,g; Figures S13

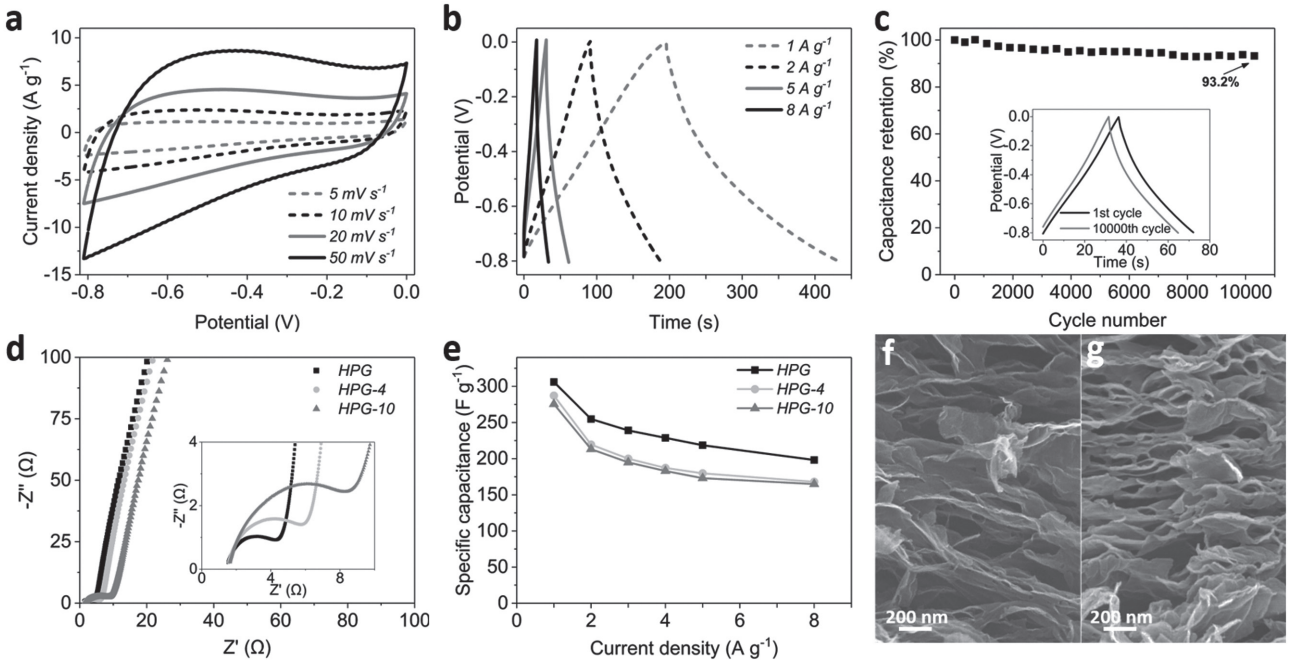

Figure 5. Supercapacitor performance of HPG, HPG-4, and HPG-10. a) CV curves of HPG at different scan rates. b) Galvanostatic charge/discharge curves of HPG at different current densities. c) Cyclic stability of HPG for 10 000 cycles at the current density of 5.0 A g^{-1}. Inset: comparative galvanostatic charge–discharge curves initial and after 10 000 cycles. d) Nyquist curves of HPG, HPG-4, and HPG-10. Inset: magnified view of the high-frequency region. e) Comparison of specific capacitance of HPG, HPG-4, and HPG-10 at different current densities. f,g) SEM images of HPG (f) and HPG-10 (g) at a same magnification.

and S14, Supporting Information). More specifically, when the precursor concentration is increased, there is an isotropic to nematic orientation transition for GO sheets in the solution.[50] Similarly, HPG-10 sample derived from GOS-10 yields a less porosity (Figure S15, Supporting Information). Accordingly, a definite precursor concentration-dependent capacitance is observed (Figure 5e; Table S2, Supporting Information). Both the CV and charge/discharge curves suggest a reduced capacitance in HPG-10 compared to the HPG derived from GOS (Figure S16, Supporting Information).

Overall, the results demonstrate a critical structure–performance relationship in energy storage (Figure S17, Supporting Information). The unprocessed GO flakes exhibit a 2D aligned graphenic structure due to strong van der Waals attraction. Whereas, our flash-freezing approach of GO dispersions leads to a 3D layer assembly with the characteristic wrinkles, further preventing them from aggregation. Moreover, the increased specific surface area of HPG results in an enhanced ion accessibility and distribution into the structure. The hierarchical porous architecture facilitates the rapid flow of electrolyte and hence also favorable to charge transport and storage.[56] The large pore volumes of mesopores and macropores contribute for charge storage and also act as channels for fast diffusion and transfer of ions.[7] Therefore, HPG exhibits a considerable performance improvements over other GO-based structures.

Finally, we have fabricated a HPG-based all-solid-state supercapacitor with polyvinyl alcohol (PVA)/KOH gel electrolyte since the development of wearable electronics and flexible power supply devices becomes increasingly attractive.[57] The device fabrication process is described in **Figure 6**a. Here, the solidified PVA/KOH gel not only functions as the electrolyte but also acts as the separator. Two identical electrodes with 1×1 cm^2 working area were then pressed to form a sandwich structure with a gel layer. The device is highly flexible even subjected to arbitrarily bending (Figure 6b). It exhibits an areal specific capacitance of ≈220 mF cm^{-2} at 1.0 mA cm^{-2} (equivalent to a gravimetric specific capacitance of 176 F g^{-1} based on a single HPG electrode, at 0.2 A g^{-1}), which is higher than, or comparable to, other reported flexible devices.[49,57,58] It also exhibits an areal specific capacitance of 149 mF cm^{-2} at a high current density of 50 mA cm^{-2} (Figure S18, Supporting Information), maintaining 68% of its initial value measured at 1 mA cm^{-2}. Such a rate capability in the solid-state gel is comparable to an aqueous electrolyte (67%), and can be attributed to the existence of relatively large pores in the HPG samples for effective infiltration of the PVA/KOH gel into electrodes. Furthermore, flexibility–capacitance relation of the device is carried out with CV measurements, which shows a negligible effect on the capacitive behavior under different bending angles (Figure 6c). The cyclic stability tests exhibit very little capacitance decay, only ≈10% drop is seen after 5000 cycles under various bending conditions, demonstrating the high durability and mechanical robustness of the supercapacitor (Figure 6d). Similar stability is also achieved in an acidic condition, with PVA/H_3PO_4 gel electrolyte (Figure S19, Supporting Information). The specific energy density and power density of the flexible device are summarized in a Ragone plot with respect to the commercial supercapacitors (Figure S20, Supporting Information). Furthermore, a tandem device was fabricated by connecting three supercapacitor units in series. Compared to a single supercapacitor,

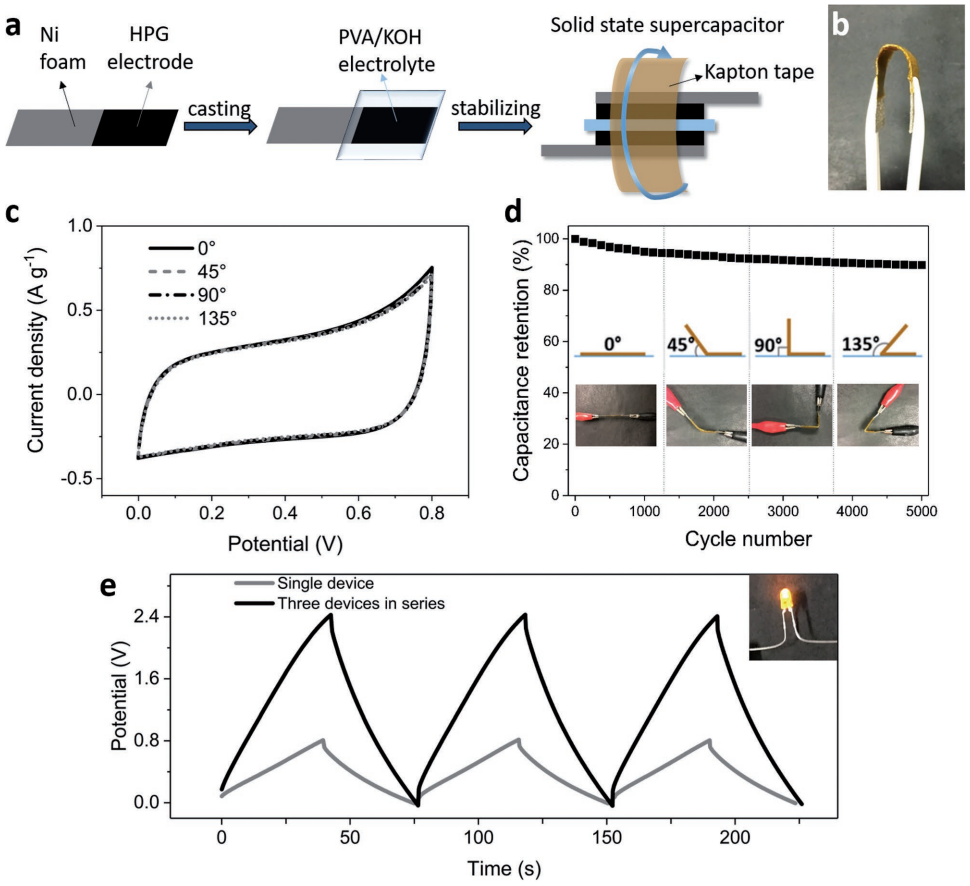

Figure 6. Fabrication and electrochemical performance of HPG-based all-solid-state flexible supercapacitor device. a) Schematic illustration of the fabrication procedure of electrode and device. b) Photograph of assembled flexible device under bending. c) CV curves of solid-state device under different bending angles, measured all at the scan rate of 10 mV s^{-1}. d) Cyclic stability test of the device under different bending conditions. e) Galvanostatic charge/discharge curves of single and three in-series HPG-based supercapacitors at 1.0 A g^{-1}. Inset: An LED powdered by tandem device.

which only operates within 0.8 V, the tandem device extended the potential window to 2.4 V with nearly unchanged charge/discharge time, indicating that the performance of each individual unit is well maintained (Figure 6e). The practical application of the device is demonstrated by lighting-up a light-emitting diode (LED, with a minimum threshold potential of 1.8 V) (Figure S18, Supporting Information).

3. Conclusions

We have demonstrated an effective synthesis strategy of producing 3D GO structures for the development of fully accessible hierarchical porous networks and thereby to enhance their performance in supercapacitors. The GOS samples prepared via the flash-freezing and freeze-dry approach of GO dispersion can effectively avoid extensive restacking and aggregation of GO sheets. Such structure shows 30–50% enhancement in their charge storage capacity compared with unprocessed GO powder samples. For example, the HPG sample, obtained from GOS under simple thermal-shock, yielded an extraordinary specific capacitance of >300 F g^{-1} at 1.0 A g^{-1}. This value is considerably higher than the reported graphene-based structures of a typical value of about 150–250 F g^{-1}. The coexistence of hierarchical pores across the microporous to mesoporous and macroporous regimes acts as charge storage reservoirs and fast ion transport channels. Therefore, HPG exhibits an excellent cyclic stability with a retention capacity of over 93% even after extended period of 10 000 cycles. Finally, a symmetric all-solid-state flexible supercapacitor constructed with the HPG sample shows an areal capacitance of 220 mF cm^{-2} at 1.0 mA cm^{-2}. Our proposed approach can effectively contribute to the further developments of GO-based structures and energy storage technologies.

4. Experimental Section

Materials: All chemicals were used as purchased without further purification. Graphite powder <20 µm (Sigma-Aldrich), potassium permanganate, ≥99.0% (Sigma-Aldrich), sulphuric acid, 95–97%, puriss (Sigma-Aldrich), phosphoric acid, ≥85 wt%,), hydrochloric acid, 35%, technical 38% (VWR), hydrogen peroxide solution, 34.5–36.5% (Sigma-Aldrich), potassium hydroxide, ≥86%, puriss, pellets (Sigma-Aldrich), poly(vinyl alcohol) 98–99% hydrolyzed (Sigma-Aldrich), poly(vinylidene fluoride) powder (Sigma-Aldrich), 1-methyl-2-pyrrolidinone, 99% (Sigma-Aldrich), and nickel foam for battery (MTI Corporation).

Synthesis of GO: GO was prepared by an improved Hummers' method as reported in the literature.[34,59] Briefly, graphite powder (1 g) was added to 9:1 mixture of concentrated H_2SO_4 and H_3PO_4

(22.5 mL:2.5 mL) under vigorous stirring at 0 °C. $KMnO_4$ (6 g) was then slowly added to the mixture under persistent stirring at a temperature below 5 °C. The mixture was then left to cool down to 0 °C and kept stirring overnight. Then the mixture was slowly heated to 50 °C in oil bath and left for another day. After that the solution turned to a brown paste. Deionized (DI) water (120 mL) was added to dilute the paste and left stirring for an hour. Subsequently, 35.5% H_2O_2 (9 mL) was added to the solution drop by drop to reduce any unreacted excess $KMnO_4$; during this the color of the solution changed to bright yellow. It was stirred for another 30 min and left for settling. Then the GO was washed by dilute HCl (3.5%) acid (750 mL) to remove remaining salts followed by washing with DI water to neutral. The GO powder sample was obtained by freeze-drying.

Preparation of GOS: As-prepared GO powder (100 mg) was dissolved in DI water (50 mL) under ultrasonication to form homogeneous solution. Then the solution was dropped into liquid nitrogen by a 2 mm diameter pipette followed by freeze-drying to obtain the GOS. In controlled experiment, a batch of samples named GOS-4 and GOS-10 were synthesized, where the numbers shown are GO solution precursor concentration (4 and 10 mg mL^{-1}).

Here it is worth noting that the speed of freezing against the volume of GO solution must be taken into consideration. As the specific heat capacity of water is high, it is very difficult to achieve a "congruent freezing" or "flash-freeze," for the high volumes of water dispersion using the liquid nitrogen or any other coolants. In this case, the ice only grows gradually from outside interface to inside, during which the layers tend to concentrate at the boundary of ice crystals and align vertically.[60,61] In order to obtain a homogeneous 3D assembly, the GO dispersion should be congruently frozen. Thus, the volume of the dispersion must be minimized. For this case, we chose to use a 2 mm diameter pipette to drop the dispersion into the liquid nitrogen, where the frozen GOS size is actually depended on the droplet size (around 2–3 mm diameter). The subsequent freeze-drying is only to remove the ice via sublimation, the size of formed GOS remains to be in the 2–3 mm diameter range.

Preparation of Simple Thermal Reduced GO (srGO) and GOS (srGOS): GO powder and obtained GOS samples were directly subjected to a slow heating rate of 2 °C min^{-1} from room temperature to 400 °C and kept for 1 h then cooled down. As obtained samples were named as simple thermal reduced GO (*sr*GO) and GOS (*sr*GOS). For comparation, the sample reduced at different temperature of 200 °C was also synthesised and named as *sr*GOS@200.

Preparation of Facile Thermal-Shock Reduced GOS (HPG): The GOS sample was placed in a glass tube and inserted in to the preheated tube furnace at 400 °C for no more than 5 min. The thermal shock occurred in less than 2 min after the sample vial put in the furnace. During this process, the bright yellow spheres turned to black color. Then the vial was kept in the furnace for another 2 min to ensure the complete reduction process. The obtained sample was named as hierarchical porous graphene networks. All samples (*sr*GO, *sr*GOS, and HPG) were directly utilized for electrochemical capacitors test and other characterizations.

Structural Characterization: The morphology and microstructure of prepared samples were performed with SEM (Jeol 6700) and TEM (Jeol). TGA and DSC analyses were carried out on Setsys from Setaram Instrument at a heating rate of 3 °C min^{-1} under N_2 atmosphere. PXRD patterns were collected by Stoe Stadi-P, Mo-K-α (wavelength of 0.71073 Å), and Cu-K-α (wavelength of 1.54056 Å). FTIR data were obtained in transmittance mode by Nicolet 6700 FTIR with background correction. XPS measurements were investigated by Al-K-α, Thermo Scientific. The N_2 adsorption–desorption isotherms were measured by Quantachrome Autosorb-iQC at 77 K. The specific surface area was calculated from isotherms based on the Brunauer–Emmett–Teller method. The pore size distribution was obtained from desorption data according to a combination of quenched solid density functional theory for micropores and mesopores <40 nm and Barrett–Joyner–Halenda method for mesopores and macropores >40 nm.

Electrochemical Characterization: CV, charge–discharge, EIS and cyclic stability tests were measured by Autolab (Metrohm PGSTAT302N) electrochemical workstation. For the three-electrode configuration, 1.0 M KOH aqueous solution was used as the electrolyte. Ag/AgCl and platinum foil used as a reference electrode and a counter electrode, respectively. The working electrode was prepared by directly compressing 1 mg activate materials (with 0.01 mg accuracy) onto 1 cm × 1 cm area of precleaned 1 cm × 3 cm nickel foams at 50 MPa for 1 min. The CV test potential range of all samples was maintained between –0.8 and 0 V and scanned at different rates between 5 and 200 mV s^{-1}. The galvanostatic charge–discharge tests were carried out in the potential window between –0.8 and 0 V with different current densities from 1.0 to 10.0 A g^{-1}. The EIS tests were performed at open circuit potential with a sinusoidal signal in a frequency range from 100 kHz to 10 mHz at an amplitude of 10 mV. The cyclic stability test was conducted for continuous 10 000 cycles at a constant charge–discharge current density of 5.0 A g^{-1}. The galvanostatic specific capacitance of the *sr*GO, *sr*GOS, and HPG samples were calculated from charge–discharge curves according to following equation: $C = (I \times \Delta t)/(m \times \Delta V)$, where C is the galvanostatic specific capacitance (F g^{-1}), I is the discharge current (A), m is the mass of the electrode material (g), Δt is the discharge time (s), ΔV is the operating discharge potential window (V) after IR-drop correction (subtracted by the V_{drop}).

For the all-solid-state supercapacitor device, PVA/KOH gel was used as electrolyte. The device was prepared as follow: First, PVA (2 g) was added to DI water (15 mL) and heated to 75 °C under vigorous stirring until the solution became clear. KOH (2 g) in DI water (5 mL) was then added dropwise into PVA solution and further stirred for 30 min. The working electrode was prepared by coating active sample on the nickel foam current collector. Typically, the mixture of active material and polyvinylidene fluoride (PVDF) with a weight ratio of 90:10 was ground with 1-methyl-2-pyrrolidinone (NMP) to form a homogenous slurry. As-prepared slurry was uniformly coated on to the 1 cm × 1 cm area among 1 cm × 3 cm nickel foam. After drying at 100 °C for 12 h, the foam was compressed at 50 MPa to form the working electrode with an active material loading of ≈2.5 mg. Next, the formed PVA/KOH solution was cast onto the electrodes and dried at room temperature for 12 h. Finally, two symmetrical electrodes were assembled together and sealed with Kapton tape to fabricate the device. The solid-state device with acidic electrolyte was fabricated by simply replacing the gel electrolyte and current collector with PVA/H_3PO_4 gel and carbon paper, respectively. The gravimetric and areal specific capacitance of device were calculated by $C_{mass} = (I \times \Delta t)/(m \times \Delta V)$ and $C_{area} = (I \times \Delta t)/(S \times \Delta V)$, respectively, where C_{mass} is the gravimetric specific capacitance (F g^{-1}), C_{area} is the areal specific capacitance (F cm^{-2}), I is the discharge current (A), m is the total mass of two electrodes, S is the geometric working area of the device (cm^2), Δt is the discharge time (s), ΔV is the discharge potential window (V) after IR-drop correction. Therefore, the gravimetric energy density (Wh kg^{-1}) and power density (W kg^{-1}) of the device were calculated by $E_{device} = (C_{mass} \times \Delta V^2)/2$ and $P_{device} = E_{device}/\Delta t$.

Supporting Information

Supporting Information is available from the Wiley Online Library or from the author.

Acknowledgements

This work was supported by the EPSRC (Grant Nos. EP/L018330/1 and EP/K002252/1).

Conflict of Interest

The authors declare no conflict of interest.

Keywords

energy storage, graphene oxide, hierarchical porous structure, supercapacitors, thermal reduction

Received: July 19, 2017
Revised: August 21, 2017
Published online:

[1] P. Simon, Y. Gogotsi, *Nat. Mater.* **2008**, *7*, 845.
[2] B. Dunn, H. Kamath, J.-M. Tarascon, *Science* **2011**, *334*, 928.
[3] F. Bonaccorso, L. Colombo, G. Yu, M. Stoller, V. Tozzini, A. C. Ferrari, R. S. Ruoff, V. Pellegrini, *Science* **2015**, *347*, 1246501.
[4] Y. Xu, Z. Lin, X. Zhong, X. Huang, N. O. Weiss, Y. Huang, X. Duan, *Nat. Commun.* **2014**, *5*, 4554.
[5] D. A. Dikin, S. Stankovich, E. J. Zimney, R. D. Piner, G. H. B. Dommett, G. Evmenenko, S. T. Nguyen, R. S. Ruoff, *Nature* **2007**, *448*, 457.
[6] Y. Hernandez, V. Nicolosi, M. Lotya, F. Blighe, Z. Sun, S. De, I. T. McGovern, B. Holland, M. Byrne, Y. Gunko, J. Boland, P. Niraj, G. Duesberg, S. Krishnamurti, R. Goodhue, J. Hutchison, V. Scardaci, A. C. Ferrari, J. N. Coleman, *Nat. Nanotechnol.* **2008**, *3*, 563.
[7] T. Lin, I.-W. Chen, F. Liu, C. Yang, H. Bi, F. Xu, F. Huang, *Science* **2015**, *350*, 1508.
[8] J. Xu, Z. Tan, W. Zeng, G. Chen, S. Wu, Y. Zhao, K. Ni, Z. Tao, M. Ikram, H. Ji, Y. Zhu, *Adv. Mater.* **2016**, *28*, 5222.
[9] S. Yun, S. Kang, S. Park, H. S. Park, *Nanoscale* **2014**, *6*, 5296.
[10] S. Chen, J. Zhu, X. Wu, Q. Han, X. Wang, *ACS Nano* **2010**, *4*, 2822.
[11] P. Pachfule, D. Shinde, M. Majumder, Q. Xu, *Nat. Chem.* **2016**, *8*, 718.
[12] L. L. Zhang, R. Zhou, X. S. Zhao, *J. Mater. Chem.* **2009**, *38*, 2520.
[13] G. He, J. Li, W. Li, B. Li, N. Noor, K. Xu, J. Hu, I. P. Parkin, *J. Mater. Chem. A* **2015**, *3*, 14272.
[14] S. Gadipelli, H. A. Patel, Z. Guo, *Adv. Mater.* **2015**, *27*, 4903.
[15] J. Zhang, Z. Xia, L. Dai, *Sci. Adv.* **2015**, *1*, e1500564.
[16] W. Qian, F. Sun, Y. Xu, L. Qiu, C. Liu, S. Wang, F. Yan, *Energy Environ. Sci.* **2013**, *7*, 379.
[17] W. Chaikittisilp, M. Hu, H. Wang, H.-S. Huang, T. Fujita, K. C.-W. Wu, L.-C. Chen, Y. Yamauchi, K. Ariga, *Chem. Commun.* **2012**, *48*, 7259.
[18] D. R. Dreyer, S. Park, C. W. Bielawski, R. S. Ruoff, *Chem. Soc. Rev.* **2010**, *39*, 228.
[19] M. F. El-Kady, Y. Shao, R. B. Kaner, *Nat. Rev. Mater.* **2016**, *1*, 16033.
[20] S. Gadipelli, Z. X. Guo, *Prog. Mater. Sci.* **2015**, *69*, 1.
[21] S. Park, R. S. Ruoff, *Nat. Nanotechnol.* **2009**, *4*, 217.
[22] S. Pei, H. M. Cheng, *Carbon* **2012**, *50*, 3210.
[23] X. Zhang, Z. Sui, B. Xu, S. Yue, Y. Luo, W. Zhan, B. Liu, *J. Mater. Chem.* **2011**, *21*, 6494.
[24] Z. Wu, Y. Sun, Y. Tan, S. Yang, X. Feng, K. Mullen, *J. Am. Chem. Soc.* **2012**, *134*, 19532.
[25] G. Srinivas, Y. Zhu, R. Piner, N. Skipper, M. Ellerby, R. Ruoff, *Carbon* **2010**, *48*, 630.
[26] G. Srinivas, J. W. Burress, J. Ford, T. Yildirim, *J. Mater. Chem.* **2011**, *21*, 11323.
[27] Y. Xu, K. Sheng, C. Li, G. Shi, *ACS Nano* **2010**, *4*, 4324.
[28] X. Yang, J. Zhu, L. Qiu, D. Li, *Adv. Mater.* **2011**, *23*, 2833.
[29] G. He, M. Qiao, W. Li, Y. Lu, T. Zhao, R. Zou, B. Li, J. A. Darr, J. Hu, M. M. Titirici, I. P. Parkin, *Adv. Sci.* **2017**, *4*, 1600214.
[30] Y. Xu, C. Chen, Z. Zhao, Z. Lin, C. Lee, X. Xu, C. Wang, Y. Huang, M. I. Shakir, X. Duan, *Nano Lett.* **2015**, *15*, 4605.
[31] D. Voiry, J. Yang, J. Kupferberg, R. Fullon, C. Lee, H. Y. Jeong, H. S. Shin, M. Chhowalla, *Science* **2016**, *3398*, 1.
[32] Y. Zhu, S. Murali, M. D. Stoller, K. J. Ganesh, W. Cai, P. J. Ferreira, A. Pirkle, R. M. Wallace, K. a Cychosz, M. Thommes, D. Su, E. a. Stach, R. S. Ruoff, *Science* **2011**, *332*, 1537.
[33] Q. Du, M. Zheng, L. Zhang, Y. Wang, J. Chen, L. Xue, W. Dai, G. Ji, J. Cao, *Electrochim. Acta* **2010**, *55*, 3897.
[34] S. Gadipelli, Y. Lu, N. T. Skipper, T. Yildirim, Z. Guo, *J. Mater. Chem. A* **2017**, *5*, 17833.
[35] Y. Zhu, S. Murali, M. D. Stoller, A. Velamakanni, R. D. Piner, R. S. Ruoff, *Carbon* **2010**, *48*, 2118.
[36] J. Xia, F. Chen, J. Li, N. Tao, *Nat. Nanotechnol.* **2009**, *4*, 505.
[37] J. Luo, H. D. Jang, T. Sun, L. Xiao, Z. He, A. P. Katsoulidis, M. G. Kanatzidis, J. M. Gibson, J. Huang, *ACS Nano* **2011**, *5*, 8943.
[38] M. D. Stoller, S. Park, Z. Yanwu, J. An, R. S. Ruoff, *Nano Lett.* **2008**, *8*, 3498.
[39] Y. Yoon, K. Lee, C. Baik, H. Yoo, M. Min, Y. Park, S. M. Lee, H. Lee, *Adv. Mater.* **2013**, *25*, 4437.
[40] U. N. Maiti, J. Lim, K. E. Lee, W. J. Lee, S. O. Kim, *Adv. Mater.* **2014**, *26*, 615.
[41] K. Xie, X. Qin, X. Wang, Y. Wang, H. Tao, Q. Wu, L. Yang, Z. Hu, *Adv. Mater.* **2012**, *24*, 347.
[42] C. X. Guo, C. M. Li, *Energy Environ. Sci.* **2011**, *4*, 4504.
[43] C. Li, X. Zhang, K. Wang, X. Sun, G. Liu, J. Li, H. Tian, J. Li, Y. Ma, *Adv. Mater.* **2017**, *21*, 1604690.
[44] L. L. Zhang, X. Zhao, M. D. Stoller, Y. Zhu, H. Ji, S. Murali, Y. Wu, S. Perales, B. Clevenger, R. S. Ruoff, *Nano Lett.* **2012**, *12*, 1806.
[45] G. Srinivas, J. Burress, T. Yildrim, *Energy Environ. Sci.* **2012**, *5*, 6453.
[46] J. Zhao, Y. Jiang, H. Fan, M. Liu, O. Zhuo, X. Wang, Q. Wu, L. Yang, Y. Ma, Z. Hu, *Adv. Mater.* **2017**, *21*, 1604569.
[47] S. H. Park, H. K. Kim, S. B. Yoon, C. W. Lee, D. Ahn, S. I. Lee, K. C. Roh, K. B. Kim, *Chem. Mater.* **2015**, *27*, 457.
[48] Z. Lei, J. Zhang, L. L. Zhang, N. A. Kumar, X. S. Zhao, *Energy Environ. Sci.* **2016**, *9*, 1891.
[49] Y. Shao, M. F. El-kady, C. Lin, G. Zhu, K. L. Marsh, J. Y. Hwang, Q. Zhang, Y. Li, H. Wang, R. B. Kaner, *Adv. Mater.* **2016**, *28*, 6719.
[50] J. Luo, H. D. Jang, J. Huang, *ACS Nano* **2013**, *7*, 1464.
[51] G. Srinivas, C. A. Howard, S. M. Bennington, N. T. Skipper, M. Ellerby, *J. Mater. Chem.* **2009**, *19*, 5239.
[52] D. Krishnan, F. Kim, J. Luo, R. Cruz-Silva, L. J. Cote, H. D. Jang, J. Huang, *Nano Today* **2012**, *7*, 137.
[53] M. Winter, R. J. Brodd, *Chem. Rev.* **2004**, *104*, 4245.
[54] S. Gadipelli, T. Zhao, S. A. Shevlin, Z. Guo, *Energy Environ. Sci.* **2016**, *2*, 1050.
[55] M. F. El-Kady, V. Strong, S. Dubin, R. B. Kaner, *Science* **2012**, *335*, 1326.
[56] N. Jackel, P. Simon, Y. Gogotsi, V. Presser, *ACS Energy Lett.* **2016**, *1*, 1262.
[57] Y. Xu, Z. Lin, X. Huang, Y. Liu, Y. Huang, X. Duan, *ACS Nano* **2013**, *7*, 4042.
[58] Z. Weng, Y. Su, D. W. Wang, F. Li, J. Du, H. M. Cheng, *Adv. Energy Mater.* **2011**, *1*, 917.
[59] D. C. Marcano, D. V. Kosynkin, J. M. Berlin, A. Sinitskii, Z. Sun, A. Slesarev, L. B. Alemany, W. Lu, J. M. Tour, *ACS Nano* **2010**, *4*, 4806.
[60] L. Qiu, J. Z. Liu, S. L. Y. Chang, Y. Wu, D. Li, *Nat. Commun.* **2012**, *3*, 1241.
[61] P. Zhang, J. Li, L. Lv, Y. Zhao, L. Qu, *ACS Nano* **2017**, *11*, 5087.